

# Solar wind predictions for the Parker Solar Probe orbit

## Near-Sun extrapolations derived from an empirical solar wind model based on Helios and OMNI observations

M. S. Venzmer and V. Bothmer

University of Goettingen, Institute for Astrophysics, Friedrich-Hund-Platz 1, 37077 Göttingen, Germany

First draft 9 August 2016; first changes 21 June 2017; received date; accepted date

### ABSTRACT

**Context.** In view of the planned near-Sun spacecraft mission Parker Solar Probe (PSP) (formerly Solar Probe Plus) the solar wind environment for its prime mission duration (2018–2025) and down to its intended closest perihelion (9.86 solar radii) is extrapolated using in situ data. The PSP mission will be humanity’s first in situ exploration of the solar corona. Visiting this yet uncharted region is of special interest, because it will help answer hitherto unresolved questions on the heating of the solar corona and the source and acceleration of the solar wind and solar energetic particles. The solar wind extrapolation of this study is performed within the project CGAUSS (Coronagraphic German And US Solar Probe Survey) which is the German contribution to the PSP mission as part of the Wide field Imager for Solar PRobe (WISPR).

**Aims.** We present an empirical solar wind model for the inner heliosphere which is derived from Helios and OMNI in situ data. The German-US space probes Helios 1 and Helios 2 flew in the 1970s and observed solar wind in the ecliptic within heliocentric distances of 0.29–0.98 au. The OMNI database at NASA’s Space Physics Data Facility (SPDF) consists of multi-spacecraft intercalibrated in situ data obtained near 1 au. The solar wind model is used together with sunspot number predictions to estimate the frequency distributions of major solar wind parameters PSP will encounter during its mission.

**Methods.** The model covers the solar wind’s magnetic field strength and its plasma parameters proton density, velocity and temperature. Their individual frequency distributions are represented with lognormal functions. In addition, we also consider the velocity distribution’s bi-componental shape, consisting of a slower and a faster part. The model accounts for solar activity and for solar distance dependency by shifting of these lognormal distributions. We compile functional relations to solar activity by correlating and fitting the frequency distributions with the sunspot number (SSN), using almost five solar cycles of OMNI data. Further, based on the combined data set from both Helios probes, the parameters’ frequency distributions are fitted with respect to solar distance to obtain power law dependencies. Finally, by combining the found solar cycle and solar distance relations, we obtain a simple dynamical solar wind model for the inner heliosphere, confined to the ecliptic region.

**Results.** The inclusion of SSN predictions and the extrapolation to the PSP perihelion region enables us to estimate the solar wind environment for PSP’s planned trajectory during its prime mission duration 2018–2025. The estimated solar wind median values during PSP’s first perihelion are 87 nT, 340 km s<sup>-1</sup>, 4015 cm<sup>-3</sup> and 503 000 K. The modeled values for PSP’s closest perihelia are 943 nT, 290 km s<sup>-1</sup>, 9733 cm<sup>-3</sup> and 1 930 000 K, where these velocity and temperature values are clearly overestimated in comparison with existing observations.

**Conclusions.** This empirical model shows that solar wind acceleration and heating processes below 20 solar radii limit a simple back-extrapolation from existing in situ measurements.

**Key words.** solar wind – sun: heliosphere – sun: corona

### 1. Introduction

From observations of cometary tail fluctuations Biermann (1951) inferred the presence of a continuous flow of particles from the Sun. With his theoretical solar wind model Parker (1958) formulated the existence of the solar wind even before the first satellites measured it in situ in 1962 (Neugebauer & Snyder 1966) + ref. to Russian measurements. The idea of a space mission flying through the solar corona dates back to the founding year of NASA in 1958 (McComas et al. 2008). Since then several space missions have measured the solar wind in situ at a wide range of heliocentric distances, in the case of Voyager 1 as far away as 138 au in July 2017<sup>1</sup>, having even left the heliopause into interstellar space at a distance of 121 au (Gurnett et al. 2013). Until today various spacecraft have provided

a wealth of solar wind measurements near Earth’s orbit, with Wind (ref.), ACE (ref.) and DSCOVR (ref.) still orbiting around the L1 point 1.5 million km ahead of Earth in the sunward direction. Additional measurements at other distances were provided by planetary missions to Venus and Mercury, such as PVO (ref.) or MESSENGER (ref.). Ulysses was the first probe that orbited the Sun out of the ecliptic plane and thus could measure solar wind at polar latitudes (McComas et al. 1998). The nearest in situ solar wind measurements to date were obtained by the Helios mission. The in 1974 launched Helios 1 spacecraft reached distances of 0.31 au, Helios 2 launched two years later and approached the Sun up to 0.29 au (Rosenbauer et al. 1977). The NASA Parker Solar Probe<sup>2</sup> (PSP), formerly Solar Probe Plus, with a planned launch date in mid 2018, will reach after six years

<sup>1</sup> <https://voyager.jpl.nasa.gov/>

<sup>2</sup> <http://parkersolarprobe.jhuapl.edu/>

in 2024 its closest perihelia at a distance of 9.86 solar radii ( $R_{\odot}$ ), that is, 0.0459 au (Fox et al. 2015). This distance will be achieved through seven Venus gravity assists with orbital periods of 88–168 days. In its prime mission time 2018–2025 PSP provides 24 orbits with perihelia inside 0.25 au (Fox et al. 2015). Even its first perihelion, 93 days after launch in 2018, will take PSP to an unprecedented distance of 0.16 au ( $35.7 R_{\odot}$ ). **In comparison, the ESA Solar Orbiter mission with a planned launch in 2019 will have a closest perihelion of 0.289 au (ref.).**

The key PSP science objectives are to “trace the flow of energy that heats and accelerates the solar corona and solar wind, determine the structure and dynamics of the plasma and magnetic fields at the sources of the solar wind, and explore mechanisms that accelerate and transport energetic particles” as stated in Fox et al. (2015). To achieve these goals, PSP has four scientific instruments on board: FIELDS for the measurements of magnetic fields and AC/DC electric fields (Bale et al. 2016), SWEAP for the measurements of flux of electrons, protons and alphas (Kasper et al. 2016), ISOIS for the measurement of solar energetic particles (McComas et al. 2016) and WISPR for the measurement of coronal and inner heliospheric structures (Vourlidas et al. 2016).

The study presented in this paper is undertaken in the Coronagraphic German And US Solar Probe Survey (CGAUSS) project, which is the German contribution to the PSP mission as part of the Wide field Imager for Solar PRobe (WISPR). WISPR will contribute to the PSP science goals by deriving the 3D structure of the solar corona through which the in situ measurements are made to determine the sources of the solar wind. It will provide density power spectra over a wide range of structures (e.g., streamers, pseudostreamers and equatorial coronal holes) for determining the roles of turbulence, waves and pressure-balanced structures in the solar wind. It will also measure the physical properties, such as speed and density jumps of SEP-producing shocks and their CME drivers as they evolve in the corona and inner heliosphere (Vourlidas et al. 2016).

In order to help optimize the WISPR and PSP preplanning of the science operations knowledge of the expected solar wind environment is needed. For this purpose the solar wind environment is extrapolated down to the closest perihelion of  $9.86 R_{\odot}$  distance to the Sun using in situ solar wind data from the Helios probes and near 1 au data from various satellites compiled in the NASA/GSFC OMNI solar wind database.

Generally, two types of solar wind are observed in the heliosphere, slow and fast streams (Neugebauer & Snyder 1966; Schwenn 1983). Slow solar wind has typical speeds  $< 400 \text{ km s}^{-1}$  and fast solar wind has speeds  $> 600 \text{ km s}^{-1}$  (Schwenn 1990, p. 144). Their different compositions and characteristics indicate different sources and generation processes (McGregor et al. 2011b). Fast streams are found to originate from coronal holes as confirmed by Ulysses out-of-ecliptic measurements (McComas et al. 1998). The source of slow wind and its eventually different types (Schwenn 1983), is still a subject of controversial discussions because several scenarios are possible to explain its origin from closed magnetic structures in the solar corona, **such as ...intermittent reconnection at the top of streamers and pseudostreamers, coronal hole boundaries, ... (ref.)**. The occurrence frequency of these slow and fast streams varies strongly with solar activity and their interactions lead to phenomena such as stream interaction regions and for quasi-stationary coronal source regions to co-rotating interaction regions (Balogh et al. 1999). Embedded in the slow and fast solar wind streams are transient flows of coronal mass ejections (CMEs), the faster ones driving shock waves ahead (ref.). Their

rate follows the activity cycle and varies in near 1 au measurements between only one CME every couple of days during solar cycle minima up to multiple CMEs observed over several days at times of solar maxima, that is, the CME-associated flow share of the solar wind raises from about 5 % up to about 50 % (Richardson & Cane 2012).

It is not known which specific solar wind type or structure PSP will encounter at a given time during its mission, therefore we extrapolate the probability distributions of the major solar wind parameters from existing solar wind measurements and take solar cycle dependencies into account. As a baseline we describe the solar wind environment through the key quantities of a magnetized plasma: *density*, *temperature* and *magnetic field strength*. Furthermore, the bulk flow *velocity* is the defining parameter of the two types of solar wind. Solar wind quantities, like flux densities, mass flux and plasma beta, can directly be derived from these four parameters.

Our approach is to obtain analytical representations of the shapes of the solar wind parameter’s frequency distributions in Sect. 2, of their solar activity dependence in Sect. 3 and of their solar distance scaling in Sect. 4. The solar wind parameters’ frequency distributions and solar activity dependence is derived from near-Earth solar wind and sunspot number (SSN) time series with a duration of almost five solar cycles. Their distance dependency is derived from Helios solar wind measurements covering more than two third of the distance to the Sun and more than half a solar cycle. From combination of the obtained frequency distributions, SSN dependence functions and solar distance dependence functions a general solar wind model is build in Sect. 5, representing the solar activity and distance behavior. Finally, this empirical model is fed with a SSN prediction and extrapolated to PSP’s planned orbital positions in Sect. 6.

## 2. Frequency distributions of the solar wind parameters

The solar wind parameters are highly variable, due to short-term variations from structures like slow and fast wind streams, interaction regions and CMEs, whose rate and properties depend on the phase of the solar activity cycle. Hence, for deriving characteristic frequency distributions for the solar wind parameters, measurements over long-term time spans are needed. The abundance of the near-Earth hourly OMNI data set is ideally suited for this purpose, because it spans to date almost five solar cycles.

The OMNI 2 data set (King & Papitashvili 2005) combines solar wind plasma and magnetic field data collected by various satellites since 1963. This intercalibrated multi-spacecraft data is time-shifted to the nose of the Earth’s bow shock. The data is obtained from the OMNIWeb interface<sup>3</sup> at NASA’s Space Physics Data Facility (SPDF), Goddard Space Flight Center (GSFC). In this study the whole hourly data until 31 December 2016 is used, starting from 27 November 1963 (for the temperature from 26 July 1965). The data coverage of the parameters is in the range 67–74 %, corresponding to a total duration of 36–40 years. It should be noted that a test-comparison of hourly averaged with higher time resolution data for the available shorter time span 1981–2016, did not show significant differences in our results.

According to the OMNI data precision and maximal parameter ranges we specify the bin sizes to 0.5 nT for the magnetic field strength,  $10 \text{ km s}^{-1}$  for the velocity,  $1 \text{ cm}^{-3}$  for the density and  $10000 \text{ K}$  for the temperature. The frequency distributions of the solar wind magnetic field strength, proton velocity, density

<sup>3</sup> <http://omniweb.gsfc.nasa.gov/>

and temperature are shown in Fig. 1. The solar wind magnetic field strength is in the range 0.4–62 nT, the velocity in the range 156–1189 km s<sup>-1</sup>, the density in the range 0–117 cm<sup>-3</sup>, and the temperature in the range 3450–6.63 × 10<sup>6</sup> K, the mean values are at 6.28 nT, 436 km s<sup>-1</sup>, 6.8 cm<sup>-3</sup> and 1.05 × 10<sup>5</sup> K. These ranges and mean values are as statistically expected from previous analyses of near 1 au solar wind data (e.g., Table 3.3 in Bothmer & Daglis (2007, p. 39)). Much higher or lower peak values at 1 au have been observed in extraordinary events, such as the 23 July 2012 ICME with a speed of over 2000 km s<sup>-1</sup> and a peak field strength of about 100 nT that was observed by STEREO A (Russell et al. 2013) or the solar wind disappearance event observed in May 1999 with density values even down to 0.2 cm<sup>-3</sup> (Lazarus 2000).

The frequency distributions of the solar wind parameters magnetic field strength, proton density and temperature can well be approximated by lognormal distributions, whereas the proton velocity's frequency has a differing shape, as shown in Veselovsky et al. (2010). We investigate how well all four solar wind parameters' frequency distributions can be represented by lognormal functions, which we use in the process of a least squares regression fitting. The lognormal function

$$W(x) = \frac{1}{\sigma \sqrt{2\pi}x} \exp\left(-\frac{(\ln x - \mu)^2}{2\sigma^2}\right) \quad (1)$$

depends on the location  $\mu$  and the shape parameter  $\sigma$ . Changes in  $\mu$  affect both the horizontal and vertical scaling of the function whereas  $\sigma$  influences its shape. The distribution's median  $x_{\text{med}}$  and mean  $x_{\text{avg}}$  (average) positions are straightforward to interpret and are directly calculated from  $\mu$  and  $\sigma$ :

$$x_{\text{med}} = \exp(\mu) \quad \iff \quad \mu = \ln(x_{\text{med}}), \quad (2)$$

$$x_{\text{avg}} = \exp\left(\mu + \frac{\sigma^2}{2}\right) \quad \iff \quad \sigma = \sqrt{2 \ln\left(\frac{x_{\text{avg}}}{x_{\text{med}}}\right)}. \quad (3)$$

It is apparent that the mean is always larger than the median. Replacing the variables  $\mu$  and  $\sigma$  with these relations, the lognormal function (1) becomes

$$W(x) = \frac{1}{2 \sqrt{\pi \ln\left(\frac{x_{\text{avg}}}{x_{\text{med}}}\right)} x} \exp\left(-\frac{\ln^2\left(\frac{x}{x_{\text{med}}}\right)}{4 \ln\left(\frac{x_{\text{avg}}}{x_{\text{med}}}\right)}\right). \quad (4)$$

The values of  $x_{\text{med}}$  and  $x_{\text{avg}}$  obtained from fitting the individual solar wind frequency distributions are listed in Table 1.

From visual inspection, the resulting curves describe the shape of the magnetic field strength, density and temperature distributions well, as can be seen in Fig. 1. However, for the velocity the fit function appears not to be as good in describing the measured distribution's more complex shape around its maximum and in the higher velocity range. This also can be inferred from the sum of absolute residuals (SAR) between data and fit listed in Table 1, being almost three times larger than those from the other parameters.

In order to find a better fit result for the velocity distribution we assume that the velocity distribution can be made up of at least two overlapping branches (McGregor et al. 2011a). Therefore a compositional approach is chosen by combining two lognormal functions (4), involving more fit variables:

$$W_{\text{II}}(x) = c \cdot W_1(x) + (1 - c) \cdot W_2(x). \quad (5)$$

The balancing parameter  $c$  ensures that the resulting function remains normalized as it represents a probability distribution. The

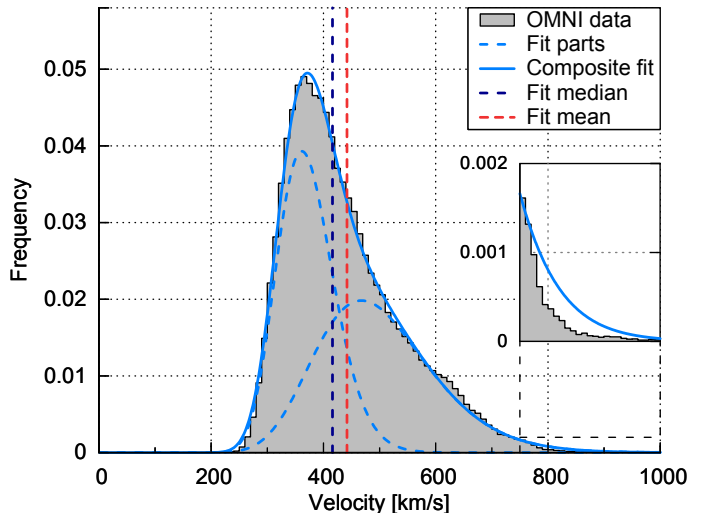


**Fig. 2.** The velocity's frequency distribution (same as in Fig. 1) and its compositional lognormal fit. The fit's median and mean values and its two fit parts are indicated as well. The inset only has a zoomed-in frequency axis, its x-axis stays the same.

fitting of  $W_{\text{II}}(x)$  to the velocity's frequency distribution yields the values of the now five fit parameters ( $c$ ,  $x_{\text{med},1}$ ,  $x_{\text{avg},1}$ ,  $x_{\text{med},2}$  and  $x_{\text{avg},2}$ ) as listed in Table 1 together with the median and mean values of the composed distribution, which can be derived via solving

$$\int W_{\text{II}}(x) dx = 0 \quad \text{and} \quad \int x W_{\text{II}}(x) dx = 0. \quad (6)$$

This more complex fit function is more accurately in describing the velocity's frequency distribution as shown in Fig. 2. Thus in the following sections we keep the double lognormal ansatz for all velocity frequency fits.

The slow and fast part contribute almost equally ( $c \approx 0.5$ ) to the long-term velocity distribution function. For the bulk of the solar wind these static lognormal functions describe the parameters' distributions well, but differ for the extreme values, mainly caused by CME events. The simple lognormal fit functions underestimate the frequency of the solar wind parameters in their high value tails, except for the temperature's tail which is overestimated as seen by the insets in Fig. 1. The velocity's compositional lognormal fit only slightly overestimates its tail as seen in the inset of Fig. 2.

### 3. Solar activity dependence of the solar wind frequency distributions

In the next step we investigate how the long-term solar wind distribution functions presented in the previous section depend on general solar activity. Therefore we examine their correlation with the sunspot number, being a commonly used long-term solar activity index and determine the time lags with the highest correlation coefficients.

The international sunspot number (1963–2016) is provided by the online catalogue<sup>4</sup> at the World Data Center – Sunspot Index and Long-term Solar Observations (WDC-SILSO), Solar Influences Data Analysis Center (SIDC), Royal Observatory of Belgium (ROB).

<sup>4</sup> <http://www.sidc.be/silso/>

**Table 1.** Resulting fit coefficients from the fitting of the lognormal function (4) to the shape of the solar wind parameters' frequency distributions from near 1 au OMNI hourly data. For the velocity also the fit parameters of the double lognormal function (5) are listed, as well as the median and mean values of the resulting velocity fit. The mean absolute errors and sums of absolute residuals are also listed. The values in brackets are the estimated standard deviations of each fit parameter.

Parameter	Median <sup>a</sup>	Mean <sup>a</sup>	Balance	MAE	SAR [%]
	$x_{\text{med}}$	$x_{\text{avg}}$	$c$		
Magnetic field	5.661(16)	6.164(18)	–	$5.51 \times 10^{-4}$	6.83
Velocity	4.085(19)	4.183(20)	–	$1.80 \times 10^{-3}$	18.69
Density	5.276(24)	6.484(34)	–	$5.49 \times 10^{-4}$	6.48
Temperature	7.470(17)	11.301(32)	–	$8.71 \times 10^{-5}$	5.78
Velocity	$W_1$ 4.89(14)	5.00(14)	0.504(62)	–	–
	$W_2$ 3.68(20)	3.72(20)	–	–	–
	$W_{\text{II}}$ 4.16(14) <sup>b</sup>	4.42(14) <sup>b</sup>	–	$3.98 \times 10^{-4}$	4.20

Notes. <sup>(a)</sup> In units of nT,  $10^2 \text{ km s}^{-1}$ ,  $\text{cm}^{-3}$  and  $10^4 \text{ K}$ . <sup>(b)</sup> Error estimates derived from the individual fit part errors.

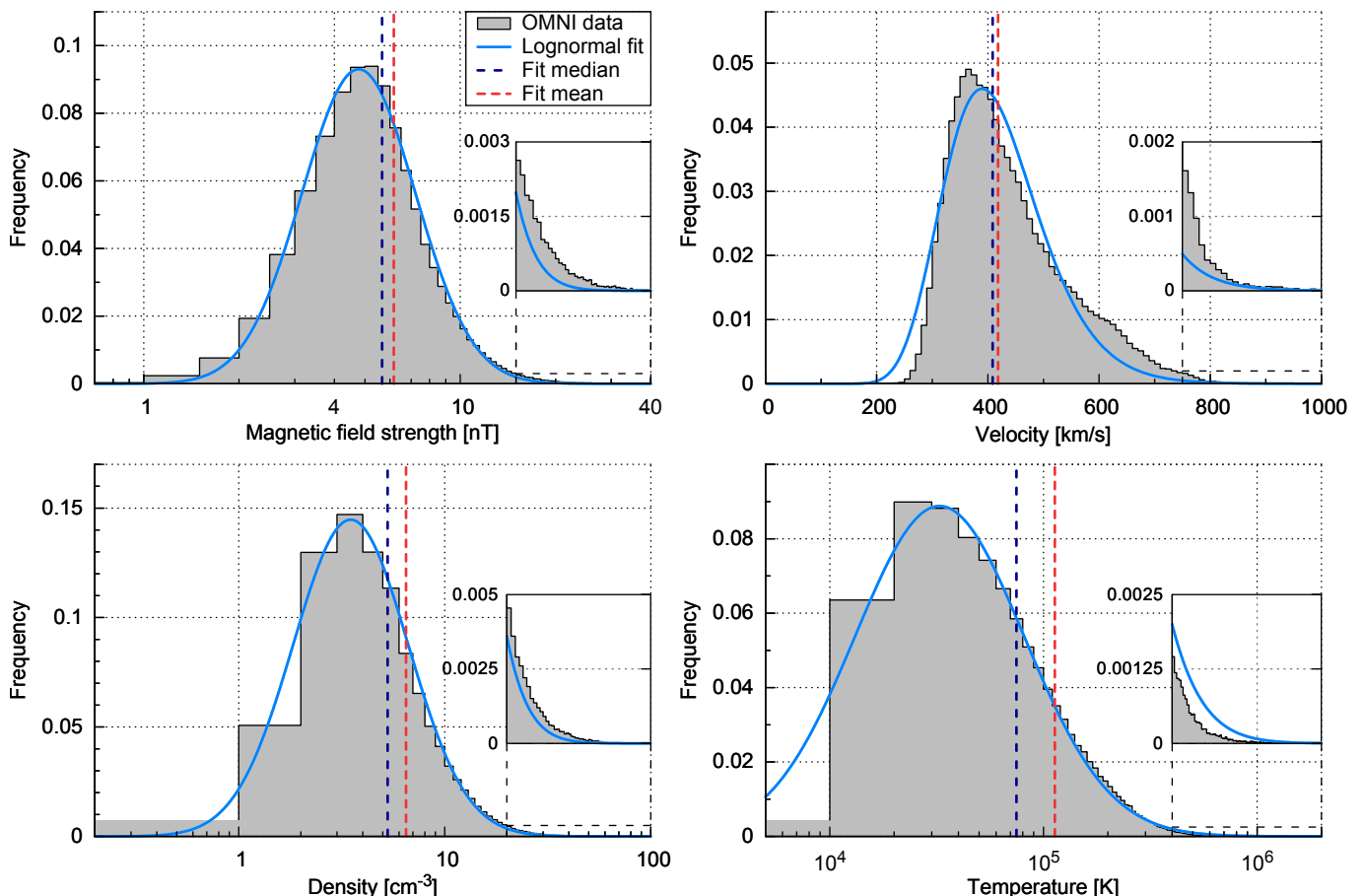


**Fig. 1.** Frequency distributions of the four solar wind parameters and their lognormal fits derived from the hourly OMNI data set. The histograms have bins of 0.5 nT,  $10 \text{ km s}^{-1}$ ,  $1 \text{ cm}^{-3}$  and  $10000 \text{ K}$ . The fit's median and mean values are indicated as well. The insets show zoomed-in frequency axes.

For the correlations we fit lognormal functions to the frequency distributions as in Sect. 2, but implement linear relations to the yearly SSN, allowing shifting of the distribution functions with SSN. For the velocity the approach is different insofar as its two components are kept fixed and instead their balance is modified with the changing SSN.

Fig. 3 shows yearly medians of the solar wind parameters and the yearly SSN together with the solar cycle number. The reason for correlating the SSN to the solar wind median values is, because the position of a lognormal function is defined by its median. The data are averaged to yearly values to avoid sea-

sonal effects during the Earth's orbit around the Sun caused by its variations in solar latitude and distance. The correlation coefficients of the solar wind parameters with the yearly SSN shown in the bottom part of Fig. 3 are calculated for time lags back to  $-15$  years to cover a time span longer than a solar cycle.

The solar wind velocity, density and temperature depend on the state of the solar cycle (Schwenn 1983). For instance the fast solar wind is correlated with the presence of polar coronal hole extensions to lower latitudes being a typical feature of the solar cycle, being the reason for the common velocity peak in the decreasing phase of the SSN, as pointed out by Bothmer & Daglis

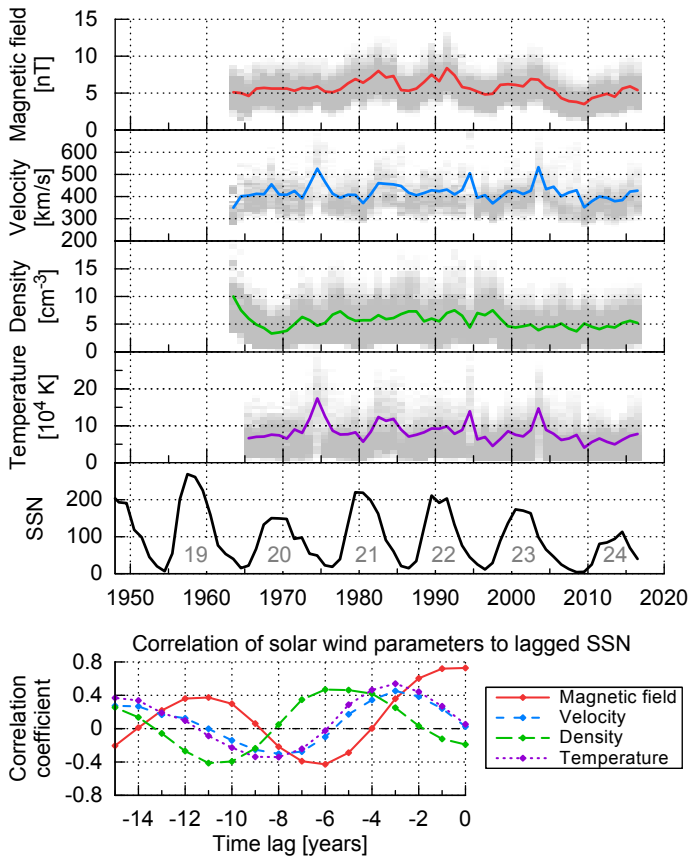


**Fig. 3.** The solar wind parameter yearly medians derived from OMNI data and the yearly SSN from the SILSO World Data Center (1963–2016) with solar cycle number (top). Their correlation coefficients with the yearly SSN are calculated for time lags back to -15 years (bottom).

(2007, p. XX, Figure XX). Therefore the solar wind velocity, density and temperature maxima exhibit time-lags to the SSN maxima.

The highest correlation coefficient of 0.728 to the SSN is found for the magnetic field strength which has no time lag. This finding is anticipated because the SSN is found to be directly proportional to the evolution of the photospheric magnetic flux (Smith & Balogh 2003). Velocity and temperature show a lag time of 3 years with peak correlation coefficients of 0.453 and 0.540. The density with a correlation coefficient of 0.468 has a lag time of 6 years, which is in agreement with the by Bougeret et al. (1984) reported density anticorrelation to the SSN. As expected, the correlation coefficients' amplitudes of all parameters decline with increasing lag time and show a frequency of about 11 years.

To enable shifts of the solar wind frequency distributions with the SSN, we add a linear SSN dependency to the median

$$x_{\text{med}}(\text{ssn}) = a_{\text{med}} \cdot \text{ssn} + b_{\text{med}}, \quad (7)$$

using a factor to the SSN  $a_{\text{med}}$  with a baseline  $b_{\text{med}}$ . We relate the mean with a scaling factor to the median to transfer its SSN dependency:

$$x_{\text{avg}}(\text{ssn}) = (1 + a_{\text{avg}}) \cdot x_{\text{med}}(\text{ssn}). \quad (8)$$

With the implementation of these relations into the lognormal function (4), the new dynamic fit function  $W'(x, \text{ssn})$  is then fitted to the yearly data. The three resulting fit coefficients ( $a_{\text{med}}$ ,  $b_{\text{med}}$  and  $a_{\text{avg}}$ ) are presented in Table 2.

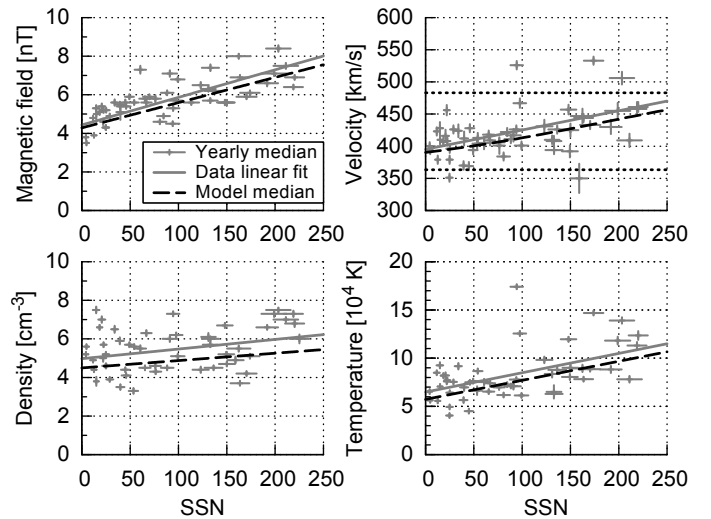


**Fig. 5.** Solar wind parameter median over lagged SSN. The yearly data medians (+) with their weighted linear fit (solid) are obtained from OMNI data. The error bars denote the SSN standard deviation and the relative weight from the yearly data coverage. The SSN dependent median (7) is derived from the lognormal model fit (dashed line). For the velocity the median is derived from the SSN weighting of the slow and fast model parts, whose magnitudes are SSN independent (dotted line).

As can be seen from Fig. 4, naturally, the fit models match with the general data trends, though single year variations are not replicated by the model (e.g., the high velocity and temperature values in 1974, 1994 and 2003). The comparison with the yearly data median values over SSN shows that the medians obtained from the modeling have a quite similar slope as shown in Fig. 5.

Again, the solar wind velocity needs a special treatment because of the double lognormal distribution (5). Since it is well known that slow and fast solar wind stream occurrence rates follow the solar cycle and basically maintain characteristic speeds (ref.), we keep the two velocity components' positions constant and vary their balance with the SSN:

$$c(\text{ssn}) = c_a \cdot \text{ssn} + c_b. \quad (9)$$

The fit result (see Table 2) yields a model in which three years after solar cycle minimum (SSN of zero) the contribution of slow solar wind to the overall solar wind distribution reaches a maximum value of about 64 % and decreases with increasing SSN as shown in Fig. 6.

To investigate the amount of slow and fast wind contributions depending on solar activity, we apply the commonly used constant velocity threshold of  $v_{\text{th}} = 400 \text{ km s}^{-1}$  (Schwenn 1990, p. 144). The linear fit to the yearly data ratio and the derived model ratio show a good agreement (see Fig. 6). Specific velocity thresholds between slow and fast solar wind cannot be directly compared with the to some degree steeper balance parameter of the double fit function used in this model. However, it appears being likely a more realistic approach than just taking a specific velocity threshold for the slow and fast wind, in agreement with the overlapping nature of the velocity flows reported by (McGregor et al. 2011a).

#### 4. Solar distance dependency

In order to derive heliocentric distance relationships of the bulk solar wind distribution functions, we apply and fit a power law

**Table 2.** Resulting fit coefficients from the OMNI data fitting with lagged SSN. For the velocity the fit parameters from the double lognormal fit and their balancing function are given. The values in brackets are the estimated standard deviation of each fit parameter.

Parameter	Median <sup>a</sup>		Mean <sup>a</sup>	Balance	
	SSN factor $a_{\text{med}}$	Baseline $b_{\text{med}}$		Scaling factor $a_{\text{avg}}$	SSN factor $c_a$
Magnetic field	$1.309(19) \times 10^{-2}$	4.285(17)	$8.786(78) \times 10^{-2}$	—	—
Density	$3.81(25) \times 10^{-3}$	4.495(26)	$3.050(27) \times 10^{-1}$	—	—
Temperature	$1.974(26) \times 10^{-2}$	5.729(19)	$6.541(28) \times 10^{-1}$	—	—
Velocity	$W'_1$ $W'_2$	— —	3.633(12) 4.831(81)	$1.008(37) \times 10^{-2}$ $2.31(20) \times 10^{-2}$	$-1.799(95) \times 10^{-3}$ 0.638(32)

Notes. <sup>(a)</sup> In units of nT,  $10^2 \text{ km s}^{-1}$ ,  $\text{cm}^{-3}$  and  $10^4 \text{ K}$ .

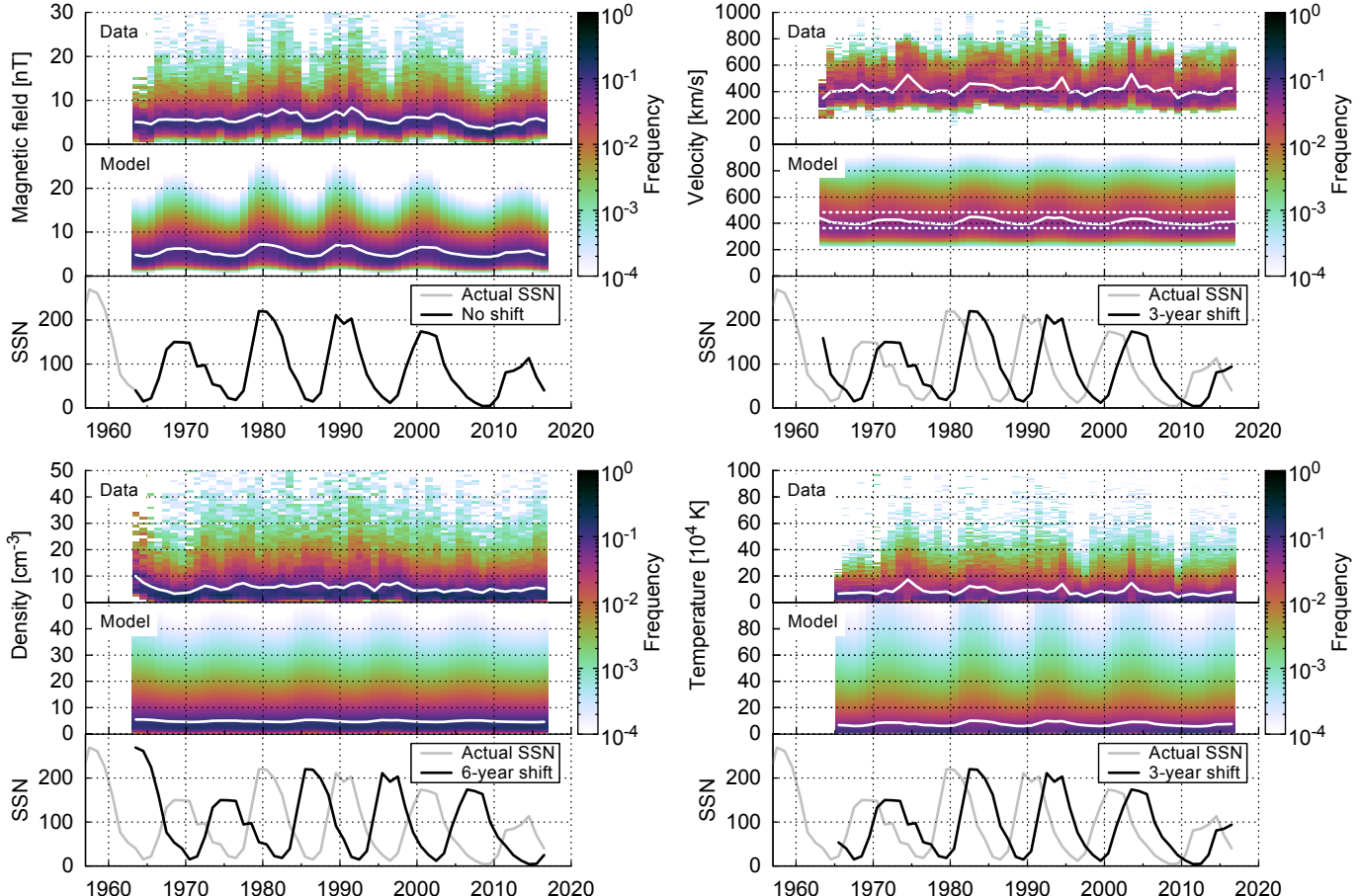


**Fig. 4.** Solar wind parameter data frequencies, lognormal fit models with their median values (white) and the corresponding yearly SSN (grey) over the OMNI time period 1963–2016. The for the models shifted SSN is indicated by a black line. The velocity median is derived from the SSN weighted constant lognormal parts (dotted).

dependency to the Helios data. We evaluate the fits’ extrapolation behavior in direction to the Sun, because in a subsequent step it will be extrapolated to the PSP orbit. We use the fitting methods of Sect. 2 for the distance-binned combined data from both Helios probes. Helios’ highly elliptical orbits in the ecliptic covered a solar distance range of 0.31–0.98 au in case of Helios 1 and 0.29–0.98 au in case of Helios 2. Launched during solar cycle minimum, the data of both probes cover the rise to the maximum of cycle 21, covering  $\sim$ 6.5 years at varying distances to the Sun.

In the same way as the OMNI data we investigate hourly averages of the Helios data. The Helios 1 merged hourly data from the magnetometer and plasma instruments (Rosenbauer et al. 1977) include  $\sim$ 12.5 orbits for the time range 10 December 1974 until 14 June 1981, those for Helios 2 include  $\sim$ 8 orbits for the

time span 1 January 1976 until 4 March 1980. The data are retrieved from the Coordinated Data Analysis Web (CDAWeb) interface at NASA’s GSFC/SPDF<sup>5</sup>.

The Helios 1 magnetometer data coverage for this data set is about 43 % (i.e., 2.8 years), that of Helios 2 amounts to 54 % (i.e., 2.3 years). The plasma data coverage is 76 % (i.e., 5.0 years) in case of Helios 1 and 92 % (i.e., 3.9 years) in case of Helios 2. Thus, using this data, one has to keep in mind that its time coverage is unequally distributed over the solar cycle. Considering the data gap distributions, the amount of data during solar cycle minimum up to mid 1977, that is, the transition from minimum to maximum, covers about 68 % whereas during maximum of cycle 21 data are available only 38 % of the time.

<sup>5</sup> <http://spdf.gsfc.nasa.gov/>

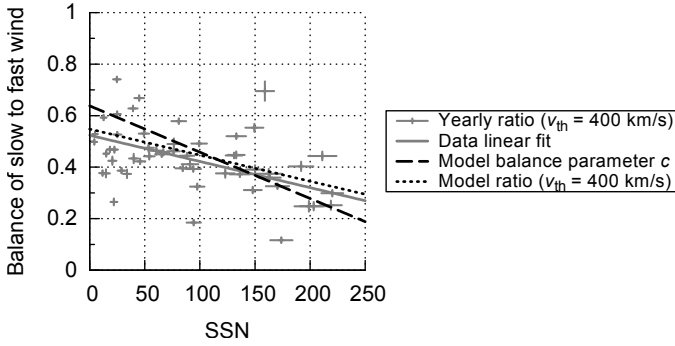


**Fig. 6.** Ratio of slow to fast solar wind for a by 3 years lagged SSN. The yearly ratios (+) and their weighted linear fit (solid line) are obtained from OMNI data with a threshold velocity of  $v_{\text{th}} = 400 \text{ km s}^{-1}$ . The error bars denote the SSN standard deviation and the relative weight from the yearly data coverage. The model's balance parameter (9) and derived ratio (same threshold) are plotted as dashed and dotted lines.

This Helios data bias towards solar minimum is the reason why in this study the OMNI solar wind data are used instead to derive long-term frequency distributions and solar cycle dependencies for the key solar wind parameters.

The median and mean values of the key solar wind parameters for different solar distances of the Helios data are calculated for the minimal distance resolution of the data set, which is 0.01 au. Assuming a radial solar wind outflow, it is expected that the distance dependence of the solar wind parameters over the Helios data range 0.29–0.98 au can be described through power law scaling. Therefore we use the power function

$$x(r) = d r^e \quad (10)$$

for the regression fit of the median and mean, with  $r$  being the solar distance. The fits are weighted through the different data counts per bin. With  $r$  in astronomical units we derive the fit coefficients ( $d_{\text{med}}$ ,  $d_{\text{avg}}$ ,  $e_{\text{med}}$  and  $e_{\text{avg}}$ ) as listed in Table 3.

As anticipated, the derived exponents agree with those found in existing studies from the Helios observations: Mariani et al. (1978) derived the exponents for the magnetic field strength separately for the fast and the slow solar wind as  $B_{\text{fast}} \propto r^{-1.54}$  and  $B_{\text{slow}} \propto r^{-1.61}$ . The velocity exponent matches with the values found by Schwenn (1983, 1990), who derived the distance dependencies for both Helios spacecraft separately as  $v_{\text{H1}} \propto r^{0.083}$  and  $v_{\text{H2}} \propto r^{0.036}$ . The calculated density exponent agrees well with the Helios plasma density model derived by Bougeret et al. (1984), yielding  $n \propto r^{-2.10} \text{ cm}^{-3}$ . The temperature exponent is similar to those in the studies by Hellinger et al. (2011, 2013), who also derived the exponents separately for the fast and the slow solar wind:  $T_{\text{fast}} = \propto r^{-0.74}$  and  $T_{\text{slow}} = \propto r^{-0.58}$ .

Fig. 7 shows the radial dependence of the solar wind parameters over the distance range 0.29–0.98 au and the mean and median values and their respective power law fits. The mean and median velocity fit exponents are very similar, which indicates that they just as well can be kept identical so that the basic shape of the frequency distribution does not change with distance. Contrary, the mean and median fits for the magnetic field strength cross each other at 0.339 au and the mean is lower than the median at smaller distances (Table 3). Thus, below that distance the distribution function cannot well be described anymore by a lognormal function. The fits for the proton temperature show a similar behavior, having an intersection at 0.082 au. Therefore the extrapolation of the magnetic field and temperature distribution frequencies to the PSP orbit by applying lognormal functions

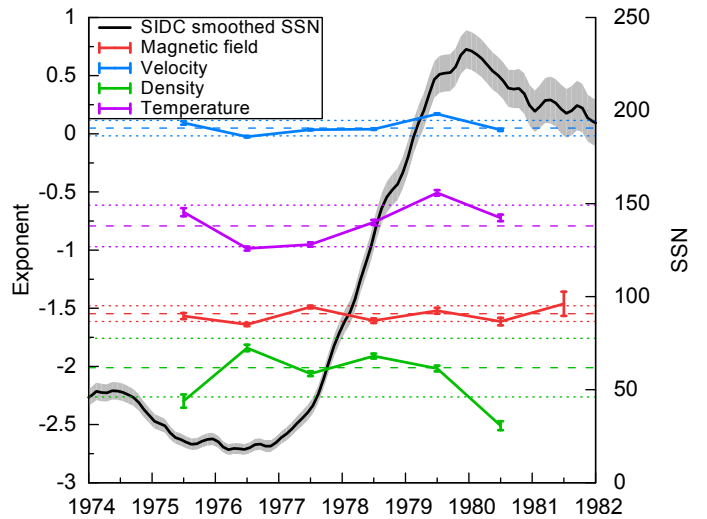


**Fig. 9.** Helios yearly variation of the solar wind parameters' fit exponents together with the SIDC 13-month smoothed monthly SSN. In this plot the year 1974 is omitted because of merely 21 days since Helios launch that year.

is limited. To circumvent such limitations we set the exponents  $e_{\text{med}}$  and  $e_{\text{avg}}$  to be identical for all four parameters. It should be noted that this simplification leads to slightly larger modeling errors, especially in case of the magnetic field strength.

Next we retrieve the frequency distributions of the four parameters in distance bins of 0.01 au, choosing the same resolution as for the OMNI data analyzed in Sect. 2—the distributions are plotted in Fig. 8. For simplification, as mentioned before, we treat the exponents of the median and average fit functions as being identical. Implementing the power law distance dependency (10) into the lognormal function (4), we get the fit parameters ( $d'_{\text{med}}$ ,  $d'_{\text{avg}}$  and the common exponent  $e'$ ). Again, we use the double lognormal function (5) for the velocity distribution fit, resulting in  $W''_{\text{II}}(x, r)$ . The additional fit parameters are the balancing parameter  $c'$  and for the second lognormal part  $d'_{\text{med},2}$  and  $d'_{\text{avg},2}$ . The resulting fit coefficients for the four solar wind parameters are presented in Table 4.

The velocity balancing parameter  $c' = 0.557$  is in good agreement with the results for the SSN dependency (9), because with a mean SSN of 59 during the Helios time period,  $c(59) = 0.53$ , as also presented in Fig. 6.

The frequency distribution data for the four solar wind parameters with respect to the radial distance from the Sun are plotted in Fig. 8, together with their power law lognormal fits and the double lognormal fit for the velocity with their median values. Fig. 8 shows that the fits represent the data well. The model's magnetic field strength is broader around values of 40 nT at the lower distance boundary than the frequency distribution implies. This behavior is expected because of the distance independent shape approximation applied. The velocity and temperature models' upper values show a higher abundance of these values than the actual data, see zoom boxes in Figs. 1 and 2.

This established solar wind model for the radial distance dependence is representative for the time of the Helios observations around the rise of solar cycle 21. The variation of the yearly power law fits' exponents are shown in Fig. 9 together with the yearly SSN for the time period 1974–1982. It can be seen that during the Helios time period there might be some systematic variation of the exponents with solar activity—at least for the velocity and temperature. However, for simplicity we assume,

**Table 3.** Fit coefficients for the median and mean solar distance dependencies of the four solar wind parameters derived from the combined Helios 1 and 2 data. The errors in brackets are the estimated standard deviations of each fit parameter. The crossing distances indicate where the median and mean fits intersect each other. The yearly variation is the weighted standard deviation derived from all yearly fit exponents.

Parameter	Median		Mean		Crossing distance [au]	Yearly variation $\Delta e$
	$d_{\text{med}}^a$	$e_{\text{med}}$	$d_{\text{avg}}^a$	$e_{\text{avg}}$		
Magnetic field	5.377(92)	-1.655(17)	6.05(10)	-1.546(18)	0.339(11)	0.11
Velocity	4.107(28)	0.058(13)	4.356(24)	0.049(10)	$0.7(83) \times 10^3$	0.012
Density	5.61(27)	-2.093(46)	7.57(30)	-2.010(38)	0.027(73)	0.072
Temperature	7.14(23)	-0.913(39)	9.67(21)	-0.792(28)	0.082(85)	0.005

Notes. <sup>(a)</sup> In units of nT,  $10^2 \text{ km s}^{-1}$ ,  $\text{cm}^{-3}$  and  $10^4 \text{ K}$ .

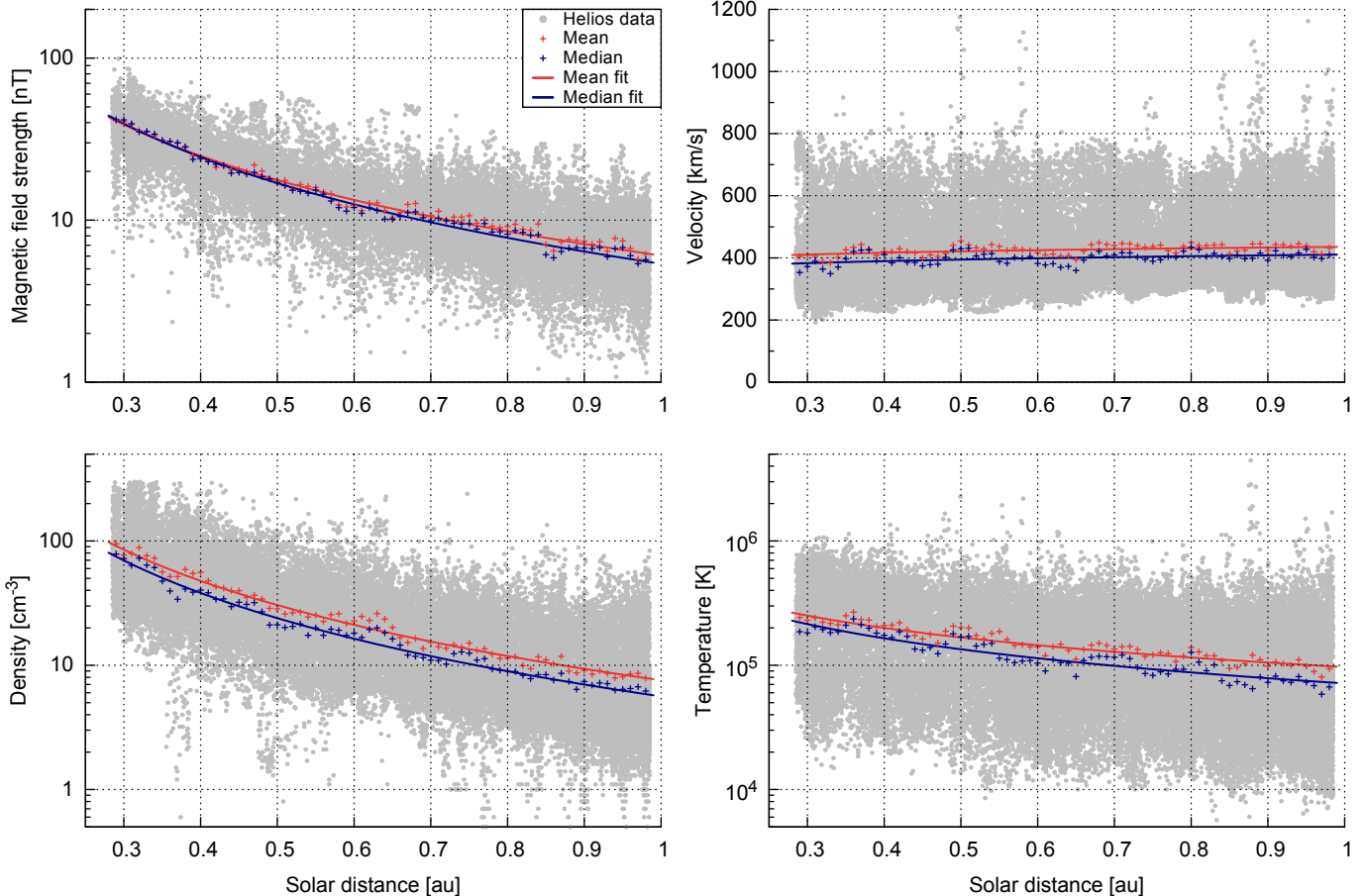


**Fig. 7.** Helios hourly data plots of the four solar wind parameters over solar distance. The mean and median per 0.01 au data bin and their fit curves are plotted as well. The Helios data has a native distance resolution of 0.01 au. To make the abundance visible in these plots, we added a random distance value of up to  $\pm 0.005$  au.

**Table 4.** Fit coefficients from the single lognormal power function, respectively double lognormal for the velocity (combined Helios data). The errors in brackets are the estimated standard deviations of each fit parameter.

Parameter	Median <sup>a</sup> $d'_{\text{med}}$	Mean <sup>a</sup> $d'_{\text{avg}}$	Exponent $e'$	Balance $c'$
Magnetic field	5.358(25)	5.705(28)	-1.662(11)	–
Density	5.424(33)	6.845(47)	-2.114(20)	–
Temperature	6.357(64)	10.72(14)	-1.100(20)	–
Velocity	$W''_1$ 5.26(13)	3.707(13)	3.748(16)	0.0990(51)
	$W''_2$ 4.13(13) <sup>b</sup>	5.42(11)	–	0.557(45)
	$W''_{\text{II}}$ 4.47(11) <sup>b</sup>	4.47(11) <sup>b</sup>	–	–

Notes. <sup>(a)</sup> In units of nT,  $10^2 \text{ km s}^{-1}$ ,  $\text{cm}^{-3}$  and  $10^4 \text{ K}$ . <sup>(b)</sup> Velocity median and mean 1 au values for the resulting function. Error estimates derived from the individual fit part errors.

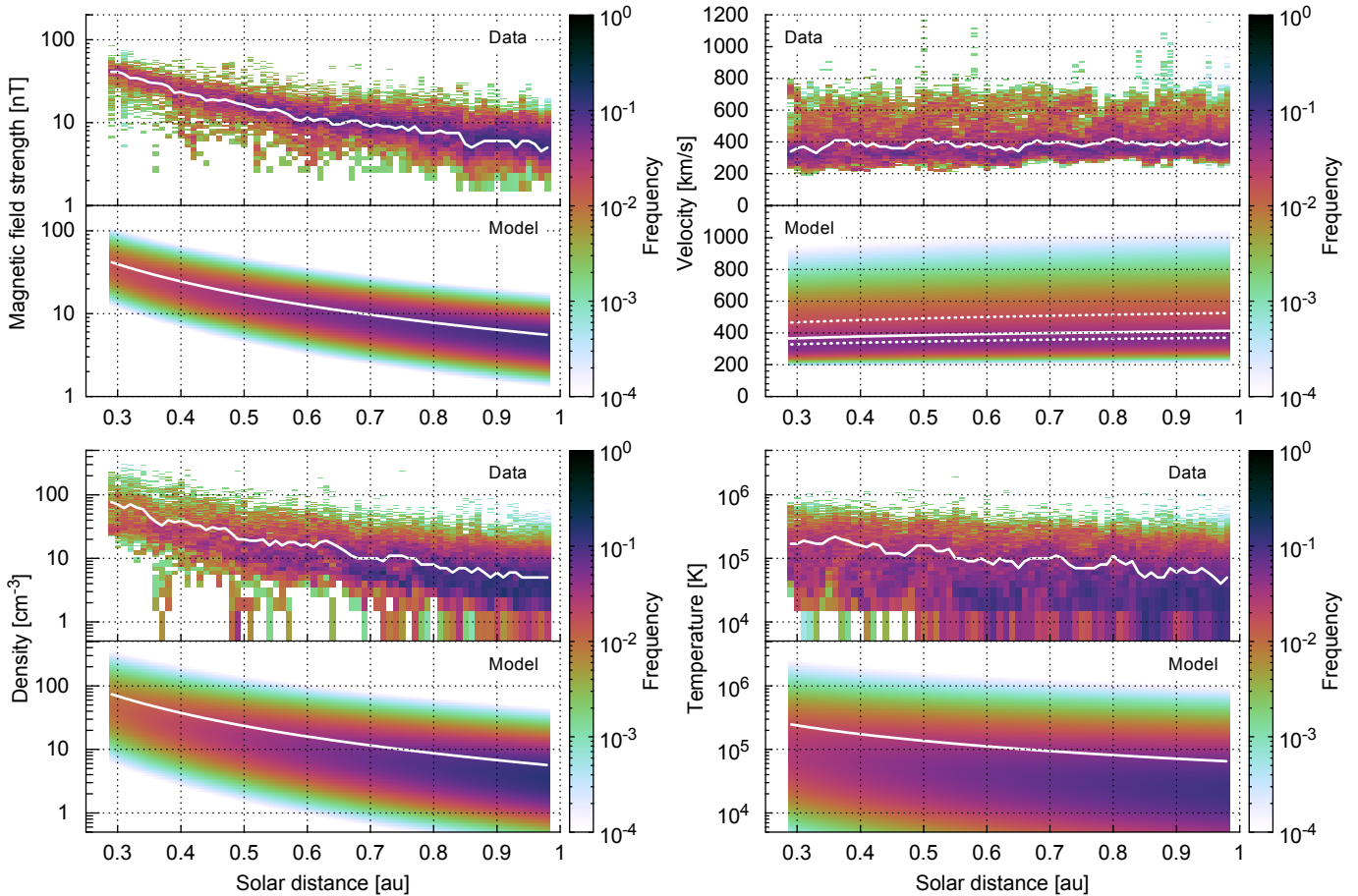


**Fig. 8.** Frequency distributions of the four solar wind parameters with respect to the solar distance. Plotted are the binned Helios data and the power law lognormal fit models with their median values (white lines). The double lognormal model is used for the velocity.

that the distance scaling laws can be treated as time independent and include the calculated exponents' yearly variations  $\Delta e$  summarized in Table 3 as relative uncertainties.

## 5. Empirical solar wind model

In order to estimate the solar wind environment for the PSP orbit, we combine the results from the solar wind frequency distributions' solar activity relationships and their distance dependencies derived from the OMNI and Helios data. The result is an empirical solar wind model for the inner heliosphere which will then be extrapolated to the PSP orbit in Sec. 6.

Since we neglect possible variations of the distance scaling laws, we combine the frequency distribution's median solar activity dependency (7) derived for 1 au from the OMNI data with the power law exponents (10) derived from the Helios data:

$$x_{\text{med}}(ssn, r) = (a_{\text{med}} \cdot ssn + b_{\text{med}}) \cdot r^e \quad (11)$$

Thus we obtain the combined model function  $W'''(x, ssn, r)$  and for the velocity  $W''''(x, ssn, r)$  with the double lognormal function (5).

## 6. Model extrapolation to PSP orbit

To estimate PSP's solar wind environment during its mission time for its orbital positions, SSN predictions are included into the in the previous sections derived empirical solar wind model

and extrapolations down to the PSP perihelion region are performed.

For SSN short-term predictions several sources are available. The SIDC provides 12-month SSN forecasts<sup>6</sup> obtained from different methods (e.g., Kalman filter combined method). The SSN prediction of NOAA's Space Weather Prediction Center (SWPC) follows for the time period until end of 2019 a consensus of the Solar Cycle 24 Prediction Panel<sup>7</sup>. For the prediction of the next solar cycle we simply assume a pattern similar to the last cycle and thus shift the last cycle by 11 years. Additionally we consider as possible alternatives SSN patterns of half and twice its amplitude as shown in Fig. 10. The SSN for PSP's first perihelion will be small—certainly below 20, whereas PSP's closest perihelia, which commence at the maximum phase of cycle 25 end of 2024, will experience as of now incalculable SSN amplitudes (see Fig. 10).

Parker Solar Probe is planned to launch in mid 2018. With its first Venus flyby it will swing into Venus' orbital plane, reaching already 93 days after launch in November 2018 a first perihelion with a distance of 0.16 au. Seven additional Venus flybys allow to finally reduce its perihelion distance to a minimum of  $9.86 R_\odot$  (Fox et al. 2015) as plotted in Fig. 10.

We extrapolate the derived empirical solar wind model to PSP's orbital distance range and compare the results with those from the existing models shown in Fig. 11.

<sup>6</sup> <http://sidc.be/silso/forecasts>

<sup>7</sup> <http://www.swpc.noaa.gov/products/solar-cycle-progression>

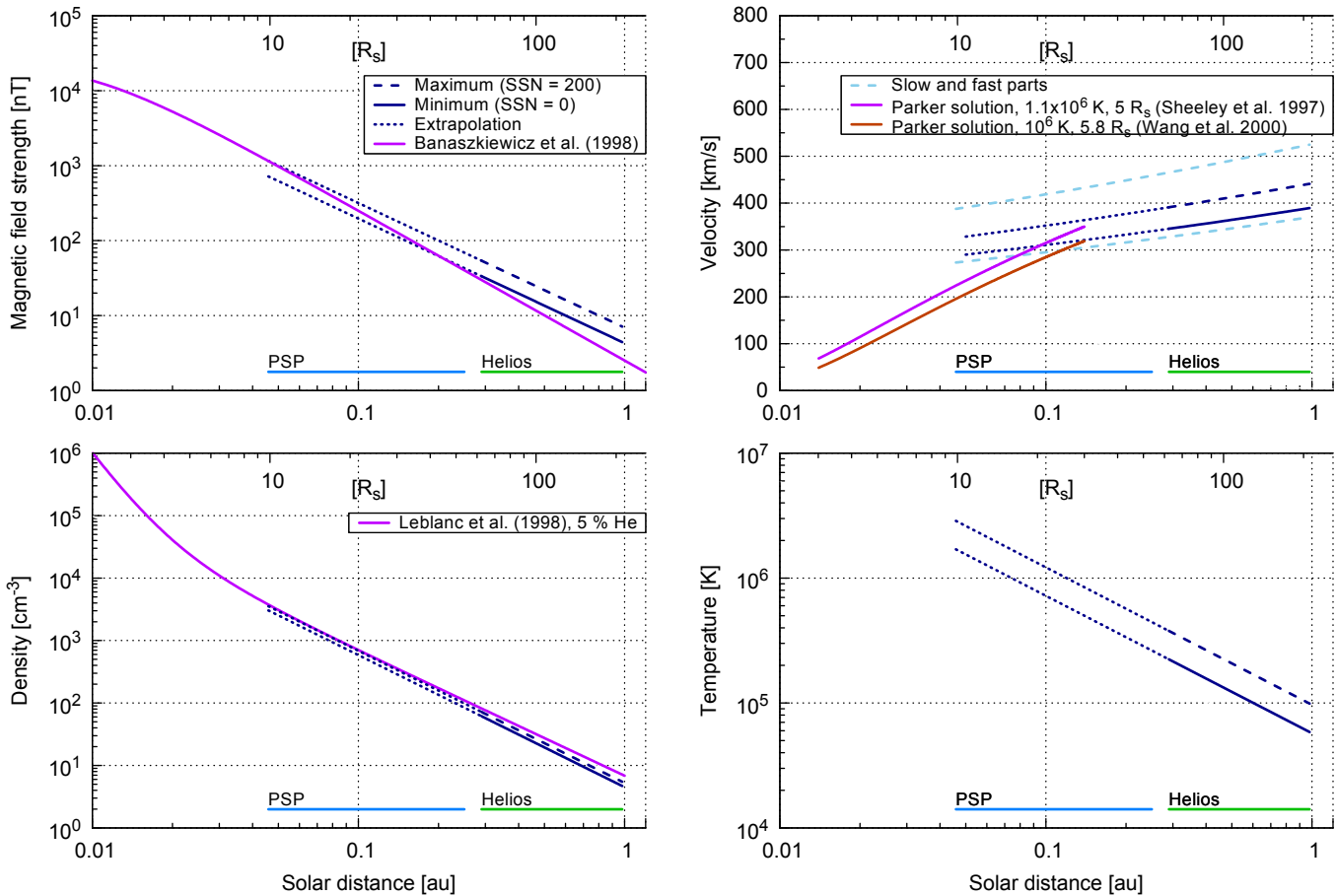


**Fig. 11.** Radial extrapolation of the solar wind parameters to the PSP orbit region. The from Helios and OMNI measurements obtained models are extrapolated to the PSP region—for the extreme cases of solar minimum (SSN = 0) and maximum (SSN = 200). Note that there is a time lag to the SSN depending on the solar wind parameter. The magnetic field radial dependence is slightly flatter than the analytic DQCS model for solar minimum which Banaszkiewicz et al. (1998) derived. Below  $20 R_\odot$  the slow wind velocity is overestimated in comparison to the measurements from Wang et al. (2000) and (Sheeley et al. 1997). They derived temperature and sonic point values for slow solar wind with the isothermal expansion model (Parker 1958). Down to PSP's perihelion the density is in good agreement with the model from Leblanc et al. (1998). to 1-column...?

The magnetic field strength is found to increase from median values of about 43 nT at 0.25 au to 715 nT at 0.046 au for a SSN of 0. Taking a SSN of 200 increases the value to 69 nT at 0.25 au and 1152 nT at 0.046 au. Our extrapolation results are slightly flatter than those derived from the analytical magnetic field model by Banaszkiewicz et al. (1998), who constructed a dipole plus quadrupole plus current sheet (DQCS) model. This difference is arguably due to the previously mentioned (Sect. 4) with solar distance changing shape of the frequency distribution, which for smaller distances deviates more from the model's log-normal distribution.

The average velocity is found to decrease from  $340 \text{ km s}^{-1}$  at 0.25 au to about  $290 \text{ km s}^{-1}$  at 0.046 au for a SSN of 0. Whereas using a SSN of 200 it decreases from  $390 \text{ km s}^{-1}$  to  $330 \text{ km s}^{-1}$ . Comparing the results with those found by (Sheeley et al. 1997) and Wang et al. (2000), who used LASCO coronagraph observations to track moving coronal features (blobs) in the distance range  $2\text{--}30 R_\odot$  to determine speed profiles and sources of the slow solar wind, shows an overestimation in our extrapolated velocity values for distances **below**  $20 R_\odot$ . Therefore, it generally can be expected that PSP will encounter a slower solar wind environment close to the Sun than our model estimates and thus it will measure solar wind acceleration processes **below**  $30 R_\odot$  (Sheeley et al. 1997; McComas et al. 2008).

The proton density increases from about  $84 \text{ cm}^{-3}$  at 0.25 au to about  $3018 \text{ cm}^{-3}$  at 0.046 au for a SSN of 0. Being almost independent of the SSN the values for a SSN of 200 are only 17 % larger. The results are in good agreement with those of Leblanc et al. (1998), who derived an electron density model from type III radio burst observations. Their model shows that the density distance dependency scales with  $r^{-2}$  and steepens just below  $10 R_\odot$  with  $r^{-6}$ . For the comparison we assumed a solar wind helium abundance of 5 %.

The extrapolated proton temperature increases from about  $260\,000 \text{ K}$  at 0.25 au to about  $1\,690\,000 \text{ K}$  at 0.046 au for a SSN of 0 and from  $440\,000 \text{ K}$  to  $2\,860\,000 \text{ K}$  for a SSN of 200. Knowing that near-Sun coronal temperatures are in the range of 2–3 MK (Billings 1959; Liebenberg et al. 1975), the model **may overestimate** the extrapolated temperatures at the PSP perihelion distance. **The results can be compared to...**

Implementing the predicted SSN for the PSP mission time and the orbital trajectory data, we can finally derive the estimated solar wind environment  $W'''(x, ssn, r)$ , to infer which solar wind parameter magnitudes can be expected.

Figs. 12 and 13 show the considered different solar wind parameters for 12 days, comprising the first perihelion in November 2018 and the closest perihelion in December 2024. In the beginning of the mission median peak values of about 87 nT,  $340 \text{ km s}^{-1}$ ,  $4015 \text{ cm}^{-3}$  and  $503\,000 \text{ K}$  are estimated to

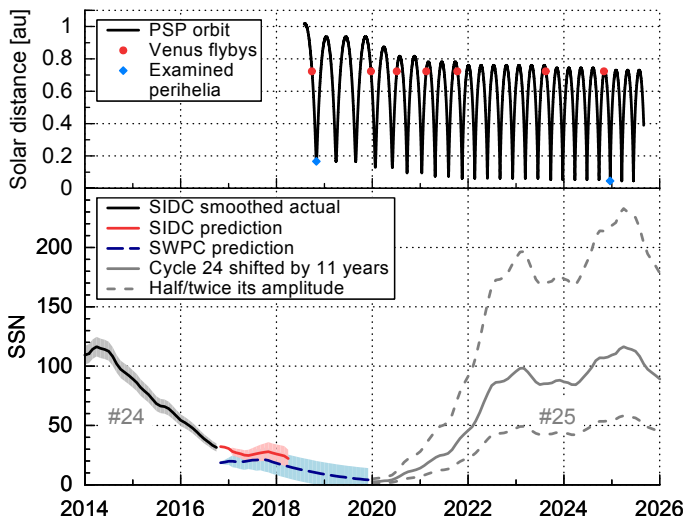


**Fig. 10.** PSP's solar distance during its mission time (top). Consecutive Venus flybys bring its perihelia nearer to the Sun. Actual and predicted SSN (bottom), that is, SIDC 13-month smoothed monthly actual SSN, SIDC prediction, SWPC prediction and simply by 11 years shifted SSN from previous cycle 24, together with two alternative trends of half and twice its amplitude.

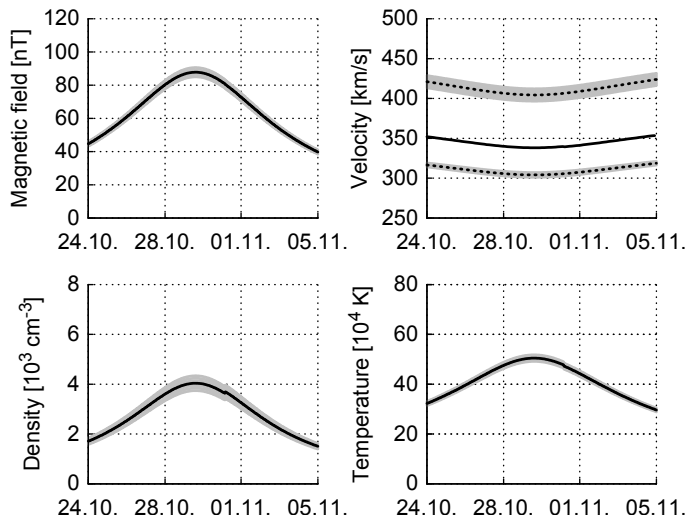


**Fig. 12.** Estimated solar wind parameter medians (black) and their error bands (grey) during 12 days in 2018 with PSP's first perihelion at about 0.16 au. For the velocity the combined median is calculated and also the SSN independent slow and fast parts are plotted (dotted).

be measured at 0.16 au, increasing to about 943 nT,  $290 \text{ km s}^{-1}$ ,  $9733 \text{ cm}^{-3}$  and  $1930000 \text{ K}$  during the closest approach at 0.046 au ( $9.86 R_\odot$ ).

XXXXXXXXXXXXXXXXXXXXXX

discuss high value zoom figures; read in Veselovsky2010

The solar wind parameters vary with solar distance as well as with latitudinal separation from the heliospheric current sheet (HCS).

The OMNI data is time-shifted to the nose of the Earth's bow shock. This leads to yearly solar distance variations of  $> 2\%$  (cite?) as the Earth orbits the Sun. Furthermore, its orbit within the ecliptic leads to a yearly variation of  $\pm 7.2^\circ$  in heliospheric latitude.

The HCS's position in latitude is highly variable around the

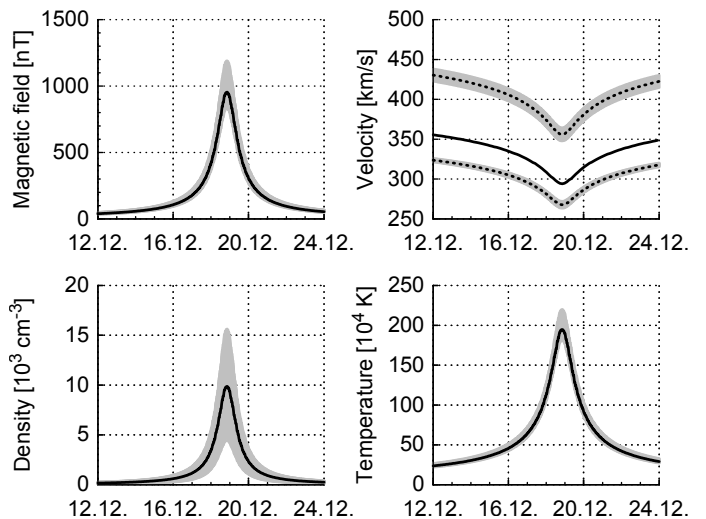


**Fig. 13.** Estimated solar wind parameter medians (black) and their error bands (grey) during 12 days in 2024 with PSP's nearest perihelion at 0.0459 au. For the velocity the combined median is calculated and also the SSN independent slow and fast parts are plotted (dotted).

solar equator (Schwenn 1990, p. 127 ff?).

Error estimation over the year (seasonal/monthly) -> we expect variations to be less than 5 %

## 7. Discussion

list of results:

- empirical solar wind model for inner heliosphere within ecliptic
- low velocity at 0.0459 au
- slow/fast ratio SSN dependency
- application validity of lognormal distributions
- > B inversion of frequency distribution
- > magnetic field distribution's with distance increasing high value tail -> source are compression regions (why with density no increase?); look into Parker1958's B-field formula...
- varying shape with distance is indicator for internal physical processes (mixing/turbulence...)

Balogh et al. (1999) p. 162 ff (origin and formation of CIRs in inner heliosphere with Helios data; latitude V dependence)

Balogh2009 (HMF review + inner heliosheath)

Aschwanden2004, p. 29

The near-Sun (PSP perihelion) solar wind velocity is expected to be slower than our model's estimates, because the position of the source (Alfvénic critical) surface is predicted to lie between 15–30 Rs (Schatten1969, Sittler1999, Exarhos2000, Katsikas2010, Goelzer2014; choose references...), up to which the solar wind is believed to be accelerated.

The Parker (1958) model of an isothermal expanding corona with a temperature of  $10^6 \text{ K}$  and a critical radius of  $5.8 \text{ R}_\odot$ .

individual velocity part discussion -> there is no specific velocity threshold between slow and fast solar wind types, the velocity ranges of both types overlap.

Not only the slowest wind but also the fastest wind is expected to converge to the average speed (Sanchez-Diaz2016 p. 2835,

using MHD-model -> very slow solar wind is continuation of slow wind) (because of interaction).

The ratio of both varies with solar activity, e.g. 3 years after maximum, polar coronal holes are observed to often have equatorial extensions (cite?). see and use Bougeret et al. (1984) p. 498...

larger influx from higher latitudes (see figure b))

approaching these regions, acceleration plays a role  
 Alfvénic critical surface i.e. source surface (see Fox before 2.1) in direction to the Sun is at about  $2.5 R_s$  the source surface (Schatten1969)  
 sonic and Alfvénic critical point positions (see Sittler & Guhathakurta (1999))  
 sonic point and slow solar wind origin (Sheeley et al. 1997)

validity and estimation of error size outside of valid model range...  
 derive heliocentric distance depending error...  
 list simplifications/approximations...  
 error estimation for general model and extreme value tendencies  
 error sources:  
 - extrapolation  
 - lognormal model  
 - SSN variance  
 all estimates outside these boundaries are extrapolations with large uncertainties.

## 8. Summary and conclusions

Further investigations should be done into structure extrapolations; outward extension of model to Mars seems feasable...

The estimated solar wind median values during PSP's first perihelion and the modeled values for PSP's closest perihelia. The velocity and temperature values are clearly overestimated below  $20 R_s$  in comparison with existing observations. This empirical model shows that solar wind acceleration and heating processes below  $20 R_s$  limit the simple back-extrapolation from existing in situ measurements.

*Acknowledgements.* This work was done within the scope of the Coronagraphic German and US SolarProbePlus Survey (CGAUSS), funded by the German Aerospace Center (DLR) under grant 50 OL 1601.

The authors thank the Helios and OMNI PIs/teams for creating and making available the solar wind in situ data. The Helios and the OMNI data are supplied by the NASA Space Science Data Coordinated Archive (NSSDCA) and the Space Physics Data Facility (SPDF) at NASA's Goddard Space Flight Center (GSFC).

Additional thanks for maintaining and providing the international sunspot number series goes to the World Data Center – Sunspot Index and Long-term Solar Observations (WDC-SILSO) at the Solar Influences Data Analysis Center (SIDC), Royal Observatory of Belgium (ROB).

The PSP SPICE kernel was kindly provided by Angelos Vourlidas.

- Bothmer, V. & Daglis, I. A. 2007, Space Weather – Physics and Effects (Praxis Publishing)
- Bougeret, J.-L., King, J. H., & Schwenn, R. 1984, Sol. Phys., 90, 401
- Fox, N. J., Velli, M. C., Bale, S. D., et al. 2015, Space Sci. Rev.
- Gurnett, D. A., Kurth, W. S., Burlaga, L. F., & Ness, N. F. 2013, Science, 341, 1489
- Hellinger, P., Matteini, L., Štverák, Š., Trávníček, P. M., & Marsch, E. 2011, Journal of Geophysical Research (Space Physics), 116, A09105
- Hellinger, P., Trávníček, P. M., Štverák, Š., Matteini, L., & Velli, M. 2013, Journal of Geophysical Research (Space Physics), 118, 1351
- Kasper, J. C., Abiad, R., Austin, G., et al. 2016, Space Sci. Rev., 204, 131
- King, J. H. & Papitashvili, N. E. 2005, Journal of Geophysical Research (Space Physics), 110, A02104
- Lazarus, A. J. 2000, Science, 287, 2172
- Leblanc, Y., Dulk, G. A., & Bougeret, J.-L. 1998, Sol. Phys., 183, 165
- Liebenberg, D. H., Bessey, R. J., & Watson, B. 1975, Sol. Phys., 44, 345
- Mariani, F., Ness, N. F., Burlaga, L. F., Bavassano, B., & Villante, U. 1978, J. Geophys. Res., 83, 5161
- McComas, D. J., Acton, L. W., Balat-Pichelin, M., et al. 2008, Solar Probe Plus: Report of the Science and Technology Definition Team, Tech. Rep. NASA/TM-2008-214161, National Aeronautics and Space Administration, Goddard Space Flight Center, Greenbelt, MD
- McComas, D. J., Alexander, N., Angold, N., et al. 2016, Space Sci. Rev., 204, 187
- McComas, D. J., Bame, S. J., Barraclough, B. L., et al. 1998, Geophys. Res. Lett., 25, 1
- McGregor, S. L., Hughes, W. J., Arge, C. N., Odstrcil, D., & Schwadron, N. A. 2011a, Journal of Geophysical Research (Space Physics), 116, A03106
- McGregor, S. L., Hughes, W. J., Arge, C. N., Owens, M. J., & Odstrcil, D. 2011b, Journal of Geophysical Research (Space Physics), 116, A03101
- Neugebauer, M. & Snyder, C. W. 1966, J. Geophys. Res., 71, 4469
- Parker, E. N. 1958, ApJ, 128, 664
- Richardson, I. G. & Cane, H. V. 2012, Journal of Space Weather and Space Climate, 2, A2
- Rosenbauer, H., Schwenn, R., Marsch, E., et al. 1977, Journal of Geophysics Zeitschrift Geophysik, 42, 561
- Russell, C. T., Mewaldt, R. A., Luhmann, J. G., et al. 2013, ApJ, 770, 38
- Schwenn, R. 1983, in NASA Conference Publication, Vol. 228, NASA Conference Publication
- Schwenn, R. 1990, Large-Scale Structure of the Interplanetary Medium, ed. R. Schwenn & E. Marsch, 99
- Sheeley, N. R., Wang, Y.-M., Hawley, S. H., et al. 1997, ApJ, 484, 472
- SILSO World Data Center. 1963–2016, International Sunspot Number Monthly Bulletin and online catalogue
- Sittler, Jr., E. C. & Guhathakurta, M. 1999, ApJ, 523, 812
- Smith, E. J. & Balogh, A. 2003, in American Institute of Physics Conference Series, Vol. 679, Solar Wind Ten, ed. M. Velli, R. Bruno, F. Malara, & B. Bucci, 67–70
- Veselovsky, I. S., Dmitriev, A. V., & Suvorova, A. V. 2010, Cosmic Research, 48, 113
- Vourlidas, A., Howard, R. A., Plunkett, S. P., et al. 2016, Space Sci. Rev., 204, 83
- Wang, Y.-M., Sheeley, N. R., Socker, D. G., Howard, R. A., & Rich, N. B. 2000, J. Geophys. Res., 105, 25133

## References

- Bale, S. D., Goetz, K., Harvey, P. R., et al. 2016, Space Sci. Rev., 204, 49
- Balogh, A., Bothmer, V., Crooker, N. U., et al. 1999, Space Sci. Rev., 89, 141
- Banaszkiewicz, M., Axford, W. I., & McKenzie, J. F. 1998, A&A, 337, 940
- Biermann, L. 1951, ZAp, 29, 274
- Billings, D. E. 1959, ApJ, 130, 961